Geophysical Journal International

Geophys. J. Int. (2010) doi: 10.1111/j.1365-246X.2010.04670.x

Earthquake source characterization by the isochrone back projection method using near-source ground motions

R. S. Jakka,[1] E. S. Cochran[1] and J. F. Lawrence[2]

[1]*Department of Earth Sciences, University of California at Riverside, Riverside,* CA 92521-0423*, USA. E-mail: rsjakka@gmail.com*
[2]*Department of Geophysics, Stanford University, Stanford,* CA 94305-2215*, USA*

Accepted 2010 May 18. Received 2010 May 13; in original form 2009 July 17

SUMMARY

Rapid and accurate assessment of source characteristics of moderate to large earthquakes is extremely useful for hazard assessment and to guide response of emergency services. Using the back projection method (BPM) it is possible to obtain an image of the source rupture process rapidly. The potential of the method in identifying the rupture propagation and its slip distribution has been shown in previous studies. However, most of the earlier back projection implementations obtain only slip intensities not slip amplitude. Here, we propose a method that is capable of providing quick estimates of the slip amplitude in addition to its distribution across the fault plane, using high frequency near-source records. First, we explore the advantages and limitations of the proposed BPM through a series of synthetic examples. We demonstrate the utility of the method to identify slip asperities and their associated intensities, with a limited number of stations (<5) distributed azimuthally around the source in the ideal case. As expected, the accuracy of asperity locations and amplitudes are improved as the number of stations increases and an appropriate station-weighting scheme is introduced. To test the BPM, we apply the method to the 2004 M_w 6.0 Parkfield earthquake using available near-source seismic data. The method identifies similar locations and amplitudes of slip using either *P*- or *S*-wave displacement records. And, for real earthquakes, we find that a significant number of observations are needed around the source to reduce the influence of local propagation and site effects.

Key words: Inverse theory; Earthquake dynamics; Earthquake source observations; Dynamics and mechanics of faulting.

GJI Seismology

1 INTRODUCTION

The back projection method (BPM) can provide a computationally inexpensive kinematic description of the source rupture process. The method does not require any prior knowledge of fault plane parameters (e.g. Kao & Shan 2007); only the hypocentre location and velocity structure of the region are needed. In comparison, earthquake source characterization using standard inversion procedures requires the calculation of complete source-station Green's functions (e.g. Olsen & Apsel 1982; Hartzell & Heaton 1983; Sekiguchi *et al.* 2002). Inverting for the Green's functions can be computationally demanding; in addition, high quality data recorded near the source and *a priori* knowledge of fault parameters are required. Below, we provide a cursory introduction to modern BPM methods and applications.

In the BPM, seismically observed displacements are back projected directly onto the fault plane of an earthquake after accounting for geometrical spreading, radiation pattern and the material properties from the source to receiver (path effects). The method provides a kinematic description of the fault rupture including slip distribution, slip amplitude (or intensity), and rupture velocity. Although there are various implementations of the BPM (e.g. Kao & Shan 2004; Ishii *et al.* 2005; Festa & Zollo 2006), the underlying concepts are similar. The BPM relies on traveltime estimates between the source and receiver, to image the earthquake rupture using seismic records. Ishii *et al.* (2005, 2007) adopted the method to trace the rupture propagation of the 2004 M_w 9.2 Sumatra–Andaman earthquake. They used the high quality teleseismic *P* records from a Hi-Net seismic array in Japan to characterize the relatively slow rupture propagation of the main shock. Walker *et al.* (2005) used the same approach to image the rupture details of 2005 M_w 8.6 Sumatra earthquake using global seismic data and obtained a high-resolution image of the rupture. Allmann & Shearer (2007) utilized *S* waves from the local strong motion velocity data recorded during the 2004 M_w 6.0 Parkfield earthquake to identify a secondary event using the BPM. In all of these studies, auto gain control was applied (normalizing records to the maximum amplitude of the record) allowing the authors to effectively ignore geometrical spreading, directivity and other amplitude effects.

Kao & Shan (2004, 2007) implemented a variation of the BPM to identify rupture plane orientation. They back project the amplitudes of the seismic envelopes using local seismic data to image the

rupture propagation on a spatial grid around the earthquake hypocentre. Festa & Zollo (2006) used the concept of isochrones to back project the amplitudes of P or S phase from near source, low-frequency bandpass filtered displacement records and retrieve slip amplitude and distribution along the fault plane. They showed the utility of the method by applying it to 2000 Tottori earthquake ($M = 6.8$) using the S phase of near source displacement records, filtered between 0.1 and 0.5 Hz. Pulido *et al.* (2008) extended the methodology of Festa & Zollo (2006) by incorporating high-frequency seismograms. They used velocity envelopes of near source P-wave velocity records and applied simple corrections for geometrical spreading and quality of records, to quickly map the asperity locations. However, they resolve only the intensity of slip or relative grid brightness on the fault plane, not the absolute amplitude of slip.

In this study, we implement the BPM similar to Pulido *et al.* (2008) with some modifications to obtain the absolute amplitude of slip, without compromising its computational efficiency. The details of the BPM are discussed in the next section. Further, the differences in the formulations of the current method and earlier isochrone BPMs (Festa & Zollo 2006; Pulido *et al.* 2008) are explained in Section 4. We investigate a series of synthetic examples to determine how the number and distribution of seismic observations can influence the recovered slip image. In addition, we explore the importance of including a correction factor for non-uniform station distribution, which can significantly influence the accuracy of results. We then apply the BPM to estimate the absolute slip amplitudes and slip distribution for the 2004 $M_{\rm w}$ 6.0 Parkfield earthquake by back projecting P and S waveforms from near-source seismograms, independently.

2 BACK PROJECTION METHOD

2.1 Calculating grid brightness

The isochrone BPM relies on the concept of isochrones introduced by Bernard & Madariaga (1984) and Spudich & Frazer (1984) to image the rupture propagation process. Isochrones are the loci of points on the rupture plane, where the radiated seismic waves reach the receiver at same time. We approximate the Green's functions using the far-field terms; this approximation is valid when direct S waves dominate the near-source waveforms, according to ray theory (Festa & Zollo 2006). Isochrone times are calculated for each seismic station and every grid point along the fault plane,

$$T_p(x_i, \xi_j) + T_r(\xi_j) = \text{Const.}, \tag{1}$$

where T_p is the traveltime for the P or S waves to reach receiver x_i from a point source (grid point on the fault plane, ξ_j). Traveltimes between each grid point to each receiver are obtained by tracing the rays through a reference 1-D model. T_r is the rupture initiation time at the grid point ξ_j. Assuming instantaneous slip or very short rupture rise time, the measured displacement at a particular time step is the slip contribution from the corresponding isochrone (Festa & Zollo 2006). Thus, the displacement amplitudes measured on the seismogram through time can be back projected on the fault plane and an image of the slip distribution can be produced.

Waveforms are initially bandpass filtered before the envelope is computed. The low frequency limit of the filter is selected such that at least two or three wavelengths exist between the station and the fault to maintain far field conditions. The high frequency limit of the filter is chosen to minimize the influence of local structures or variations over very short distances. The envelopes of P or S waveforms are computed for each station using the equation

$$V[\mathrm{d}(t)] = (\mathrm{d}(t)^2 + H^2[\mathrm{d}(t)])^{1/2}, \tag{2}$$

where $\mathrm{d}(t)$ is observed displacement record and $H[\mathrm{d}(t)]$ is the Hilbert transform of $\mathrm{d}(t)$. The instantaneous amplitude of $V[\mathrm{d}(t)]$ for each seismic station is then distributed across the fault plane along the appropriate isochrone. We account for geometrical spreading and station locations before distributing the energy across the fault plane. We neglect the influence of the source radiation pattern to minimize computational demands. Instead, we consider a large number of stations that are well-distributed radially and azimuthally around the rupture plane, which can significantly reduce the influence of stations near the nodal planes on the overall slip image. The sum of the grid brightness from each of the individual stations, normalized by number of stations, gives the final brightness or slip distribution on the rupture plane. This is expressed as

$$E_\xi = \frac{1}{N}\sum_{i=1}^{N}\left\{\sum_{k=-w/\Delta t}^{w/\Delta t} A[T_p(x_i,\xi) + T_r(\xi) + c_i + k\Delta t]\right\} \times \frac{R_{\xi i} s_i F_c}{(2W/\Delta t) n_\xi}, \tag{3}$$

where A is the envelope amplitude at a given isochrone time, c_i is the station correction time for the ith receiver, to account time shifts caused by 3-D velocity structure along the ray paths. The station correction factor is estimated from the difference between the actual arrival time observed on the seismogram and theoretical arrival time calculated by ray tracing through a 1-D velocity model. Δt is the sampling spacing of the seismic record. N is the total number of receivers used in the analysis. $R_{\xi i}$ is the source–receiver ray length, used as a correction for geometrical spreading. $2W$ is the duration of the averaging window. Envelopes are averaged to take into account uncertainties in the estimated isochrone times; ideally, the duration of the averaging window ($2W$) should be larger than the maximum expected errors in the estimated isochrone times. n_ξ is the number of grid points along an isochrone that the seismic energy, within a window of duration $2B$, is distributed over. $2B$ represents the average isochrone spacing between any two adjacent grid points; here, we consider $2W$ equal to $2B$. s_i is a factor used to account for non-uniform station distribution. F_c is a constant that accounts for the type of wave used in the analysis and is defined as follows (using a point source approximation at each grid point),

$$F_c = 4\pi\rho c^3. \tag{4}$$

In the above expression ρ and c are the approximate values of density and wave velocity (α or β for P and S waves, respectively) at the source region. The summed grid brightness expression provided above does not consider mode conversions or reflected phases.

The brightness obtained at each grid point corresponds to the time derivative of the slip function at that grid point. Assuming a simple parametrization of the slip function, the average displacement at each grid point can be computed as

$$\bar{D}_\xi = E_\xi\left[\frac{t_r}{\mu A_\xi}\right], \tag{5}$$

where μ is the shear modulus at source region, A_ξ is the area of the single grid cell, and t_r is the rise time. We approximated t_r to be the average rupture time between any two adjacent grid points. In this implementation, the effect of anelastic attenuation is not included,

as it does not significantly change the estimated slip amplitudes (<10 per cent) and is small compared to other uncertainties and simplifications (e.g. Aki & Richards 2002). Directivity effects are included in our formulation indirectly by the factor n_ξ, which scales the brightness based on the isochrones spacing (e.g. the stations that are in the direction of rupture propagation, will have larger isochrone spacing resulting in more number of grid points along each of the isochrone).

2.2 Model iterations

The final intensity image, obtained by summing the intensity contributions from all of the stations, results in a image of the fault plane in which the slip intensity is defocused, or smeared along isochrones. The defocusing is a result of the assumption that brightness is distributed uniformly along the isochrones. This effect can be reduced by iterating the model using the results of earlier back-projected images as *a priori* information (e.g. Festa & Zollo 2006). In successive iterations, slip is no longer spread uniformly along the corresponding isochrone (according to $1/n_\xi$); instead, it is distributed according to the relative brightness from the earlier iteration (i.e. the ratio of grid brightness from the previous iteration to the sum of the brightness along the isochrone). Ideally, this process is repeated until there is no significant improvement in the computed misfits. However, for real events, due to uncertainties in the velocity structure, site amplifications, and noise, iterations should be halted after a small number of iterations (typically, less than five). Continued iteration results in unrealistic slip distributions with concentrated slip patches adjacent to fault patches with zero slip.

2.3 Goodness of fit

We assess the performance of the BPM after each iteration, by comparing the back-calculated (synthetic) envelope with the observed envelope at each station using a misfit function. The synthetic envelopes for each station are back-calculated from the slip map obtained at the end of each iteration. Synthetic envelope amplitudes are determined by calculating the average value of the grid brightness over a temporal window (width $2W$) for each isochrone time, after accounting for geometrical spreading (i.e. dividing by source–receiver distance, $R_{\xi i}$). We define the misfit function as the ratio of the difference between the area under the observed and back-calculated envelopes to the area under the observed envelope. The misfit at ith station is given by,

$$misfit_i = \frac{\int |V_i(t)_{\rm obs} - V_i(t)_{\rm syn}| {\rm d}t}{\int V_i(t)_{\rm obs} {\rm d}t}, \tag{6}$$

where $V_i(t)_{\rm obs}$ is the observed envelope at ith station and $V_i(t)_{\rm syn}$ is the back calculated synthetic envelope at ith station. The average misfit at the end of a particular iteration is computed using,

$$misfit_{\rm avg} = \frac{1}{N} \sum_{i=1}^{N} misfit_i, \tag{7}$$

where N is the total number of stations used in the analysis. Misfits can further be utilized to assess the quality of the waveform data at a particular station. If the misfit of a particular station is large compared to the average misfit and increases with number of iterations, this likely indicates poor data quality and a lower weight can be assigned to that station. However, here we do not include this

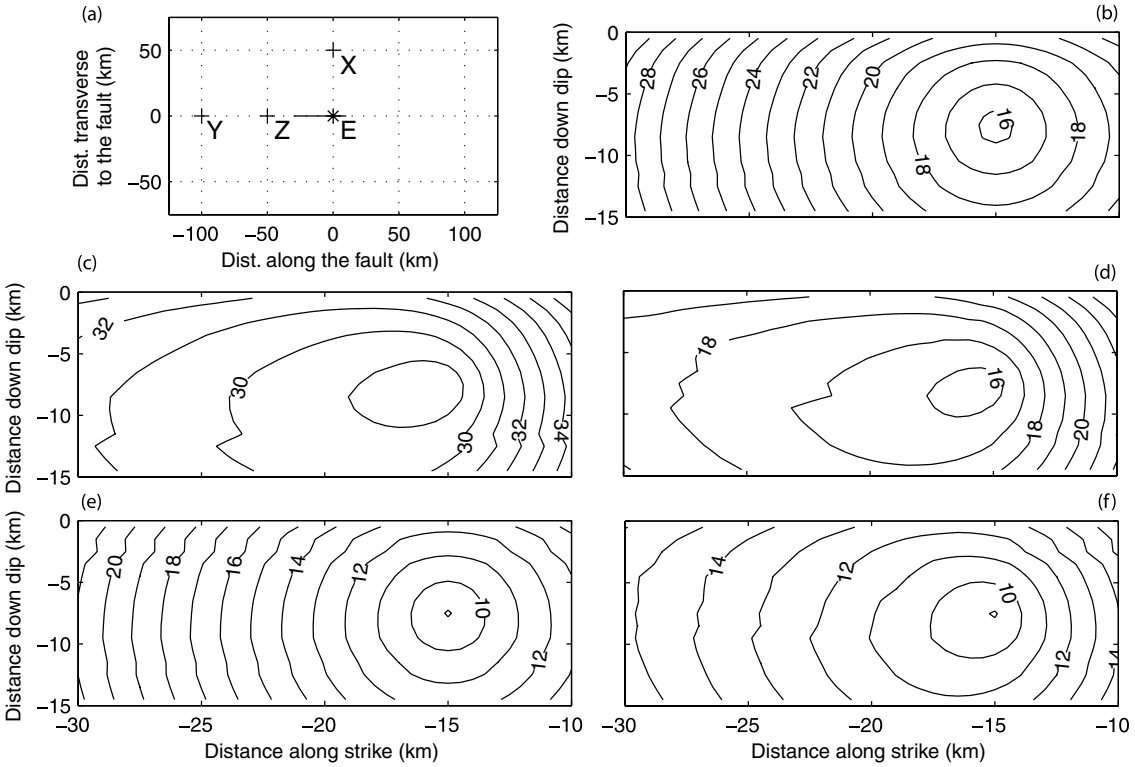

Figure 1. (a) Station locations used to compare isochrone patterns, (b) *S*-phase isochrones for station X, (c) *S*-phase isochrones for station Y, (d) *S*-phase isochrones for station Z, (e) *P*-phase isochrones for station X and (f) *P*-phase isochrones for station Z.

station quality factor to keep computational demands to minimum; the quality of an individual station becomes less important as the number of stations increases.

2.4 Estimating rupture velocity

Using the procedure discussed so far, the slip map is obtained using an assumed rupture velocity. However, it is possible to determine the best-fitting rupture velocity by examining the slip maps and average misfit for a range of rupture velocities (Festa & Zollo 2006). The optimal rupture velocity should ensure a good correlation between the observed and synthetic data (i.e. resulting in lowest average misfit) with slip focused on relatively small regions of the fault plane.

3 NON-UNIFORM STATION DISTRIBUTION CORRECTION FACTOR

Correcting for non-uniform station distribution is very important, particularly when dealing with sparsely distributed stations. The ability of the isochrone BPM to identify asperities depends upon the availability of stations with distinct isochrone patterns. If the isochrones of the available stations do not overlap significantly, then the BPM is able to accurately identify the asperities. Otherwise, the back projected energy is smeared along the isochrones. Stations that are well-distributed around the earthquake source tend to have non-overlapping isochrones resulting in improved identification and localization of energy to asperity locations. However, assigning each station with a weighting factor can reduce the smearing of energy along isochrones due to non-uniform station distribution.

Before deriving an expression for non-uniform station distribution factor, it is necessary to understand the factors that influence the isochrone shape and distribution across the fault plane. The isochrone pattern for each station is related to the station azimuth and radial distance from the source. Figs 1(b)–(f) shows the isochrones for stations shown in Fig. 1(a). From these plots, we can clearly see that the isochrones are significantly different for stations X and Z, which are located in different quadrants of the source. However, for stations at different radial distances from the source (Y and Z) the isochrones pattern is similar suggesting that a good azimuthal distribution of the observations is more important than stations at a range of distances to accurately identify the slip distribution across the fault plane.

Below we outline a station-weighting scheme that accounts for non-uniform station distribution by reducing the relative weighting of data from stations clustered around a given backazimuth. Stations at each azimuth (0–360) around the source will have different isochrone patterns irrespective of type of rupturing (e.g. unilateral or bilateral). First, we calculate the backazimuth for each station and then we determine the internal angle bisector between successive pairs of stations. Then, the station distribution factor for a given

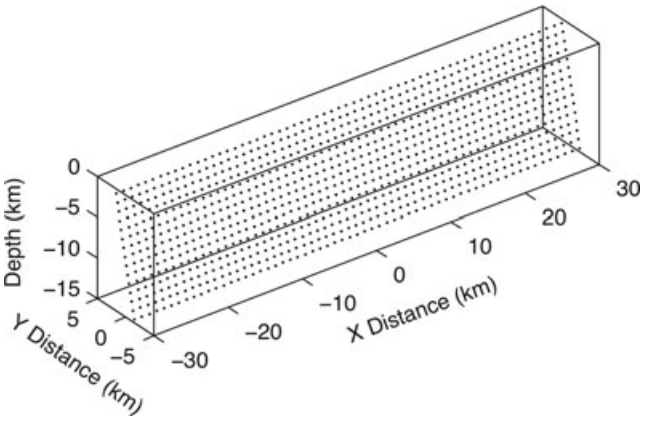

Figure 2. 3-D representation of the fault plane used in both the synthetic test and in the application of the back projection method to the Parkfield earthquake. The rupture originates at $x = 0$ and at a depth of 7.9 km. The fault plane is divided into 1 km × 1 km grids.

Table 1. Velocity structure of the Parkfield region (from Hartzell *et al.* 2007).

Thickness (km)	V_p (km s^{-1})	V_s (km s^{-1})
Southwest Side of Fault		
1	2	1.1
1	3.5	2
1	4.5	2.6
1	5.4	3.1
3	5.8	3.4
2	6.2	3.6
3	6.8	3.9
14	7	4
–	8	4.5
Northeast Side of Fault		
1	2	1.1
1	3.5	2
3	4.5	2.6
5	5.4	3.1
3	6.5	3.8
13	7	4
–	8	4.5

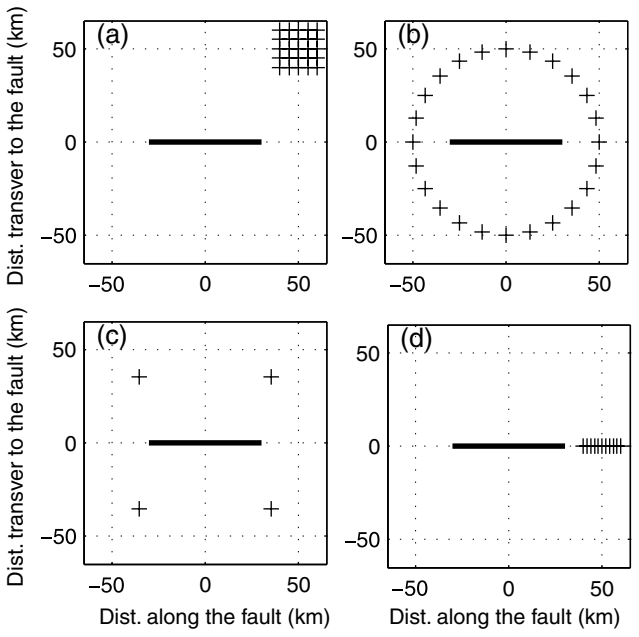

Figure 3. Station configurations used in the synthetic tests. (a) 25 stations with 5 km station spacing located in a grid in one quadrant. (b) 24 stations distributed radially around the earthquake epicentre at a distance of 50 km. (c) 4 stations distributed in each of the quadrants around the fault plane. (d) 11 station array parallel to fault strike and off the end of the rupture.

station 'i' is calculated using,

$$s_i = \sum_{j=1}^{n} \frac{\phi_{ji}}{\sum_{k=1}^{N} \phi_{jk}}, \tag{8}$$

where ϕ_{ji} is the angle between jth bisector and ith station($0 \leq \phi_{ji} < 180$). N represents number of stations. n represents number of angular bisectors between consecutive stations.

4 SUMMARY OF DIFFERENT ISOCHRONE BPM METHODS

In this section, we briefly describe previous implementations of the BPM and the modifications we introduce here. The isochrone BPM implemented by Festa & Zollo (2006) involves the evaluation of line integrals along the isochrones. For example, the observed amplitude at time t_i on the displacement record at the jth receiver is $A_j(t_i)$ and the corresponding isochrone on the fault plane is α_{ij}. Then, the slip on the fault along the isochrone α_{ij} can be obtained from the observed amplitude $A_j(t_i)$ after accounting for radiation pattern, geometrical spreading, directivity and material properties at the source and receiver region. In their method, the fault is discretized into subfaults (e.g. 1 km × 1 km regions) and isochrones are discretized ten times more finely than subfault size (length/width). Slip is then evaluated along each of isochrones within each subfault. The final slip map is obtained by summing the contributions from all of the stations. Their method is suitable for low frequency ground motions as they use absolute displacement records in their analysis. Their method is also computationally expensive as it involves the evaluation of many line integrals all along each of the isochrones.

Pulido *et al.* (2008) modified the method for use with high frequency, near source ground motions. They considered velocity envelopes and approximated various factors that account source and path effects, with simple correction factors to reduce the computational burden. Further, they considered average envelope amplitudes in their formulation to account for uncertainties in the arrival time estimates (and high frequency content). However, because they only consider relative brightness in subsequent iterations and other numerical simplifications they obtain only the intensity of slip on the fault plane.

Here, we modify the Pulido *et al.* (2008) method to determine the slip amplitude, not just intensity, and improve the method to yield a well-resolved final slip image. We use displacement envelopes from the vertical, radial, and transverse components to quickly obtain the slip distribution and its amplitude. First, we introduce a normalization factor $1/N$, which is missing in earlier implementations. This factor scales the final grid brightness by the number of observations to better represent the actual energy released during rupture. We also introduce a distribution factor $1/n_\xi$, which allows us to spread energy across all of the grid points along a particular isochrone. This factor also helps to account for directivity effects, as discussed earlier. Pulido *et al.* (2008) do not include this distribution factor, but since they normalize brightness across the fault plane with maximum grid brightness after each iteration, this does not directly affect their results. However, the omission of this distribution factor and the non-uniform station distribution factor can cause serious problems (artefacts) in the final slip map, as discussed in greater detail in Section 6. Further, there are some differences in the iterative procedures; we distribute the energy across grid points

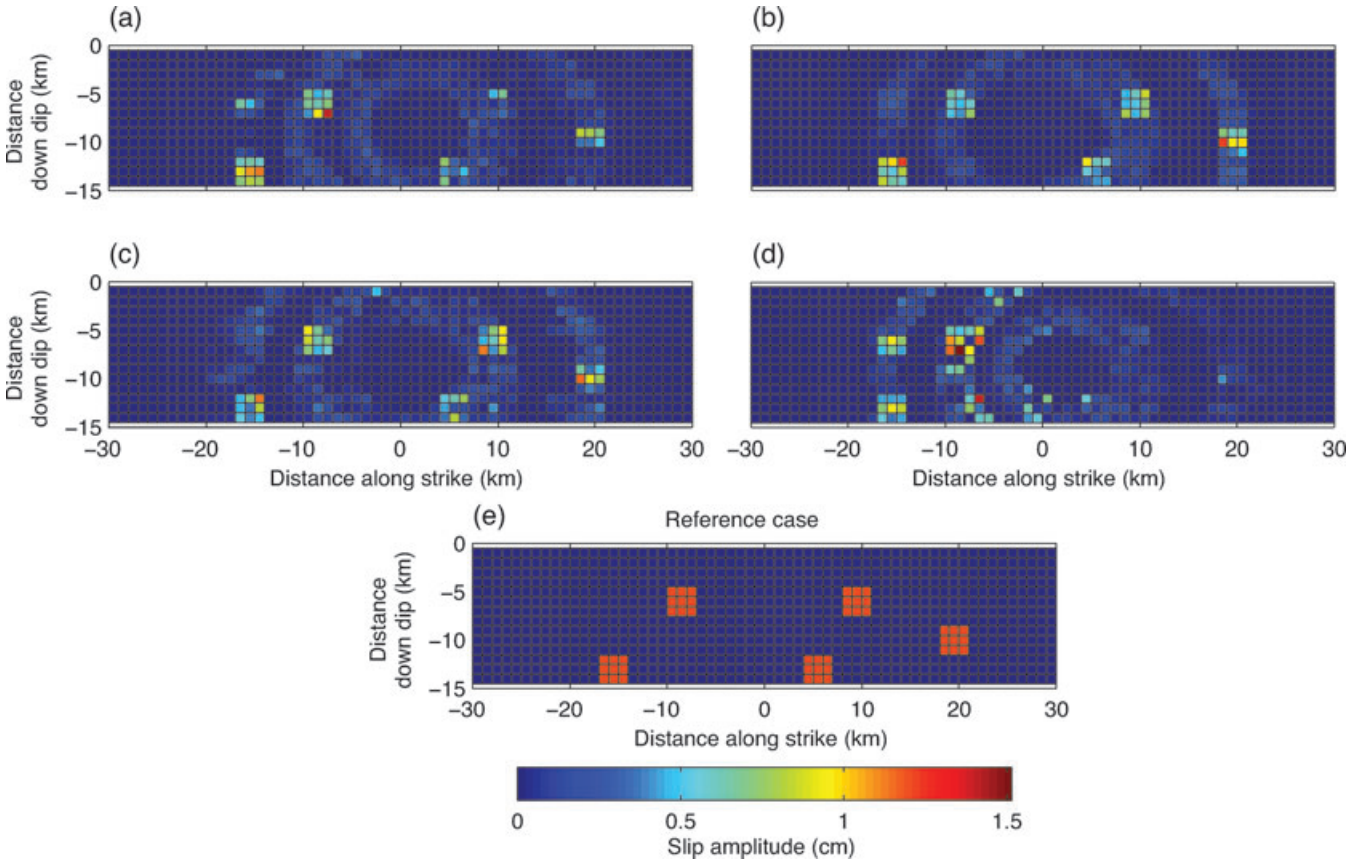

Figure 4. (a)–(d) Final slip maps after the fourth iteration obtained for the synthetic test cases using the four station configurations shown in Fig. 3. (e) Distribution and amplitude of slip used in the synthetic tests.

for each isochrone according to the relative grid brightness from the previous iteration, while Pulido *et al.* (2008) assign a weighting system based on the relative brightness of each grid point from the previous iteration.

We introduce a factor $F_{c,}$ in our formulation, which allows us to approximate the actual slip amplitudes using the final slip brightness determined at each grid point. As per the representation theorem, each of the seismic phases (*P* or *S*) is able to provide a image of slip on the fault; differences between the *P*- and *S*-phase observations are resolved using the impedance factor, F_c. We use the vertical component seismograms to determine the *P*-phase slip image. To obtain slip from the *S* phases, we consider both the horizontal components, as the *S* phases are dominant in both horizontal components of the seismogram. We rotate the horizontal components into radial and transverse directions and obtain separate slip maps from each of these components. The final slip map for the *S* phase is determined by combining the slip maps calculated from the radial and transverse component data. The use of radial and transverse components separately in the BPM analysis allows us to back calculate separate synthetic envelopes for each of the components, which are useful for assessment of the performance of the method.

Pulido *et al.* (2008) assigned a quality factor, w_i at each station, based on its epicentral distance, to minimize path effects. We do not include any quality weighting factor in our formulation, but the use of a station quality factor (as discussed above) may reduce the influence of site effects. We include a new factor s_i to account for the non-uniform distribution of stations in our BPM formulation. The importance of this factor is discussed in detail in Section 5 below and its derivation was presented in the previous section. Further, there is some ambiguity over what averaging window width ($2W$) should be used in the method. Although Pulido *et al.* (2008) used 1 s, we use a window width equal to the isochrone spacing between any two adjacent grid points. This window width allows us to track the total energy released during rupture and also better accounts for directivity.

5 SYNTHETIC TESTS OF THE BPM

We use a series of synthetic tests to explore how well the BPM identifies the location and amplitude of asperities along a fault. We model our synthetic tests on the 2004 M_w 6.0 Parkfield earthquake and implement a fault plane with a length of 60 km, width of 14 km, and dip of 77°. The fault plane is discretized into 1 km × 1 km grids (Fig. 2). To replicate the heterogeneity of an actual earthquake rupture, we model five asperities, each 3 km × 3 km in size, distributed across the fault plane (Fig. 4e).

We investigate a variety of station configurations to explore and document the influence of station distribution on the resulting slip image. Synthetic seismograms were prepared for each station by representing each asperity grid cell as a point source. The hypocentral location of the 2004 M_w 6.0 Parkfield earthquake, at 0 km along strike and at a depth of 7.9 km, is defined as the origin of the synthetic rupture. The rupture is prescribed to propagate radially with a speed of 2.8 km s^{-1} across the entire fault plane. We assume far-field conditions, so a triangular pulse centred on each grid cell of an asperity is used to approximate ground displacement (e.g. Shearer 2009). The slip amplitude at each asperity is 1.2 cm and the duration is 0.10 s. We include the effects of geometrical spreading by scaling the amplitude of the pulse by the grid-to-station distance. The traveltime of a particular energy pulse from a fault grid cell to a station is specified by the corresponding isochrone time. Isochrone times are calculated using the ray tracing program, *MacRay* (Luetgert 1992) with the 1-D *P*-wave velocity profile defined in Table 1 (Hartzell *et al.* 2007). The envelope of the final ground motion at each station is obtained by summing the contributions of all point sources from the set of five asperities.

To replicate complexities expected in actual waveform data, the amplitudes of pulses are varied randomly by up to ±20 per cent to replicate local site amplification effects and the corresponding arrival times are varied randomly by up to ±30 per cent of the pulse width to account for uncertainties in the isochrone estimates. We investigate how the number and distribution of stations can influence the resulting slip map; the various station configurations considered in this investigation are shown in Fig. 3. We implement the BPM discussed in the Section 2 and the final slip maps determined after four iterations are shown in Fig. 4. We show the results after the fourth model iteration to replicate the method used for the Parkfield earthquake.

The first case has 25 stations arranged in a small grid located in one quadrant of the rupture with 5 km station spacing, as shown in Fig. 3(a). The final slip map after four iterations is not able to adequately recover all five of the original asperities (Fig. 4a). Three of the asperities are well constrained, but two of the asperities are not fully recovered by the BPM due to lack of clear intersecting isochrones for asperities located closer to the stations. Fig. 3(b) shows the second test case with 24 stations distributed radially around the source at a distance of 50 km from the centre of the rupture plane. This station configuration recovers the location and

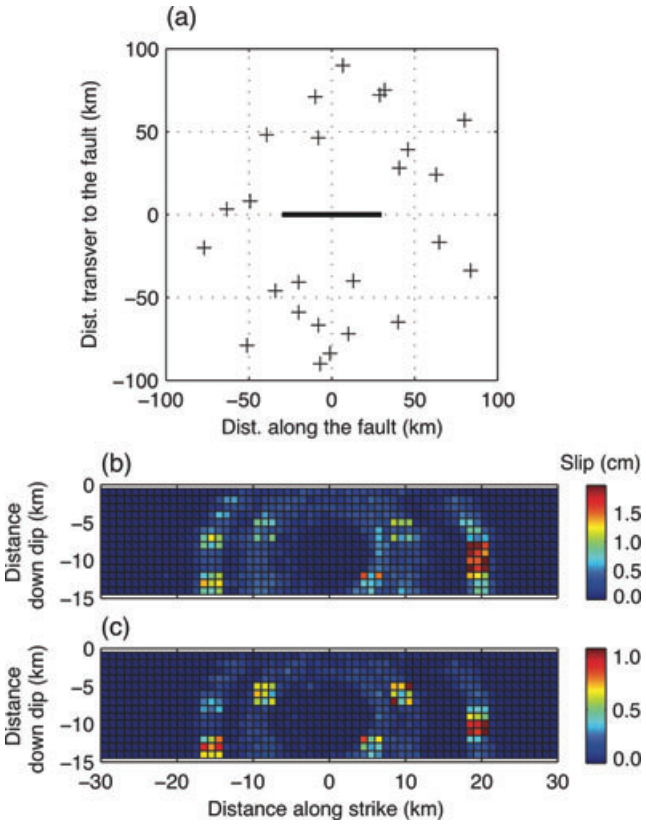

Figure 5. Synthetic test with 25 stations distributed randomly around the earthquake origin. (a) Station configuration, (b) Final slip map obtained after four iterations before applying a correction factor for non-uniform station distribution, (c) Final slip map obtained after four iterations after applying a correction factor for non-uniform station distribution.

amplitude of all asperities (Fig. 4b), demonstrating the importance of having stations distributed uniformly around the source. Next, we considered four stations distributed in each quadrant around the fault plane (Fig. 3c) to determine the influence of the number of stations on the recovery of the slip image. Although the final asperities are not as well constrained as in the previous case with 24 stations, it is able to adequately recover the location and amplitude of the five asperities (Fig. 4c). The result of this test case suggests that the station distribution is more important than the absolute number of stations. In the final test case, an array of 11 stations is aligned along a nodal plane off of the end of the fault (Fig. 3d). This test case cannot recover the asperity locations or amplitudes, further signifying the importance of good azimuthal distribution of stations. It is important to note that the synthetic cases above likely underestimate the expected uncertainties in the recovered slip maps; for an actual earthquake the slip image is expected to have higher uncertainties due to errors in computed traveltimes and local site amplifications in near-source records.

Under ideal conditions, the BPM is able to recover both the location and amplitude of slip asperities with as few as four stations distributed uniformly around the source. However, to recover the slip using actual data it is necessary to have a large number of stations distributed azimuthally around the source due to uncertainties in traveltimes, temporal and spatial averaging, and variations in amplitudes due to local site effects. To study a more realistic distribution of stations, we considered a case with 25 stations distributed randomly around the source at a distance range of 40–100 km from the centre of the fault plane, as shown in Fig. 5(a). We apply and present the back projection results before (Fig. 5b) and after (Fig. 5c) correcting for station distribution using correction factor s_i from eq. (3) above. In the case where the station distribution correction was not applied, the asperities cannot be accurately identified due to smearing along the isochrones caused by non-uniform station distribution. In contrast, when the station distribution correction is applied, the method correctly identifies all asperities. These cases demonstrate the importance of applying a station distribution correction to prevent a large number of stations in one region from dominating the final solution.

6 APPLICATION TO THE 2004 M_w 6.0 PARKFIELD EARTHQUAKE

The 2004 M 6.0 Parkfield earthquake occurred on the San Andreas Fault (SAF) in central California and was densely recorded by the General Earth Observing System (GEOS) array, the California Geological Survey (CGS) array and the U.S. Geological Survey (USGS) Parkfield dense seismograph array (Upsar). A total of 84 strong motion records are available for this earthquake within a distance of 200 km from the epicentre. However, 48 of the records were recorded within a distance of 10 km from the fault rupture (Shakal *et al.* 2005). Most of the CGS array stations are analog stations that primarily triggered on the shear wave (S) arrival. The main shock hypocentre was located at (35.818° N, 120.370° W) with a depth of 7.9 km. Previous studies of the Parkfield earthquake concluded that the rupture propagated 30 km northwest and 10 km southeast from the hypocentre (e.g. Hartzell *et al.* 2007; Ma *et al.* 2008). The fault plane extends from 0.5 km below the Earth's surface to a depth of 14.5 km, with a strike of 140° and dip of 77° (e.g. Wang *et al.* 2006). There is a considerable difference in the velocity structure

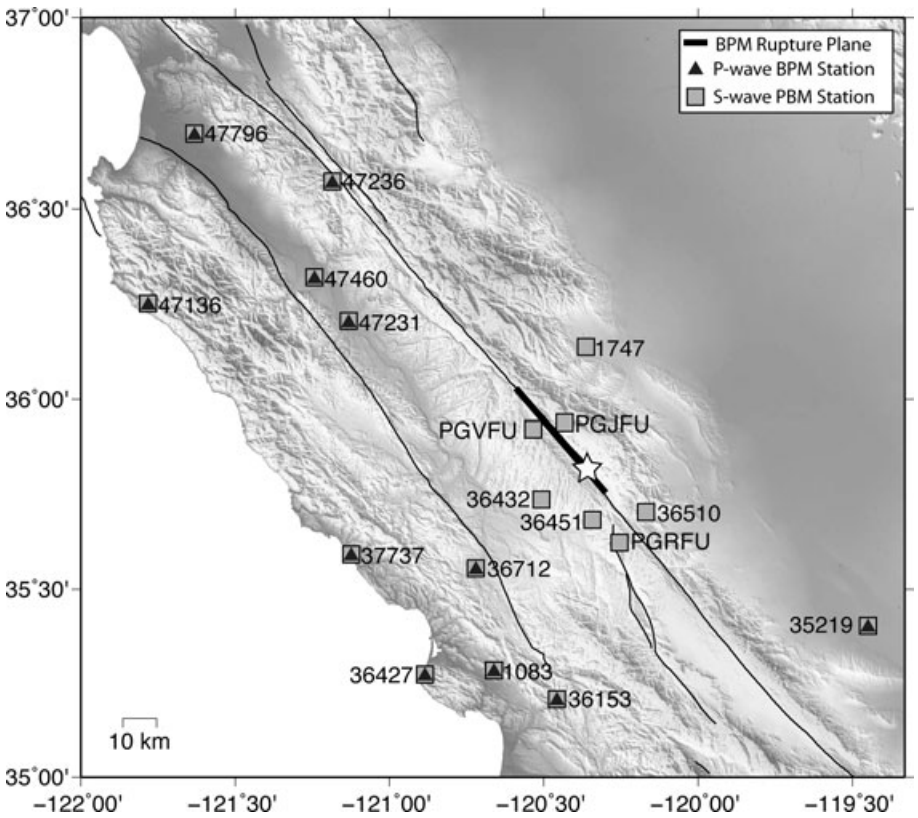

Figure 6. Station distribution around the 2004 M_w 6.0 Parkfield earthquake used in the back projection analysis. The fault plane that ruptured during the main shock is shown by the heavy black line, the main shock epicentre is shown by the star, and regional faults are shown by the thin, grey lines. Dark triangles are stations used in the *P*-wave analysis and light squares are stations used in the *S*-wave analysis.

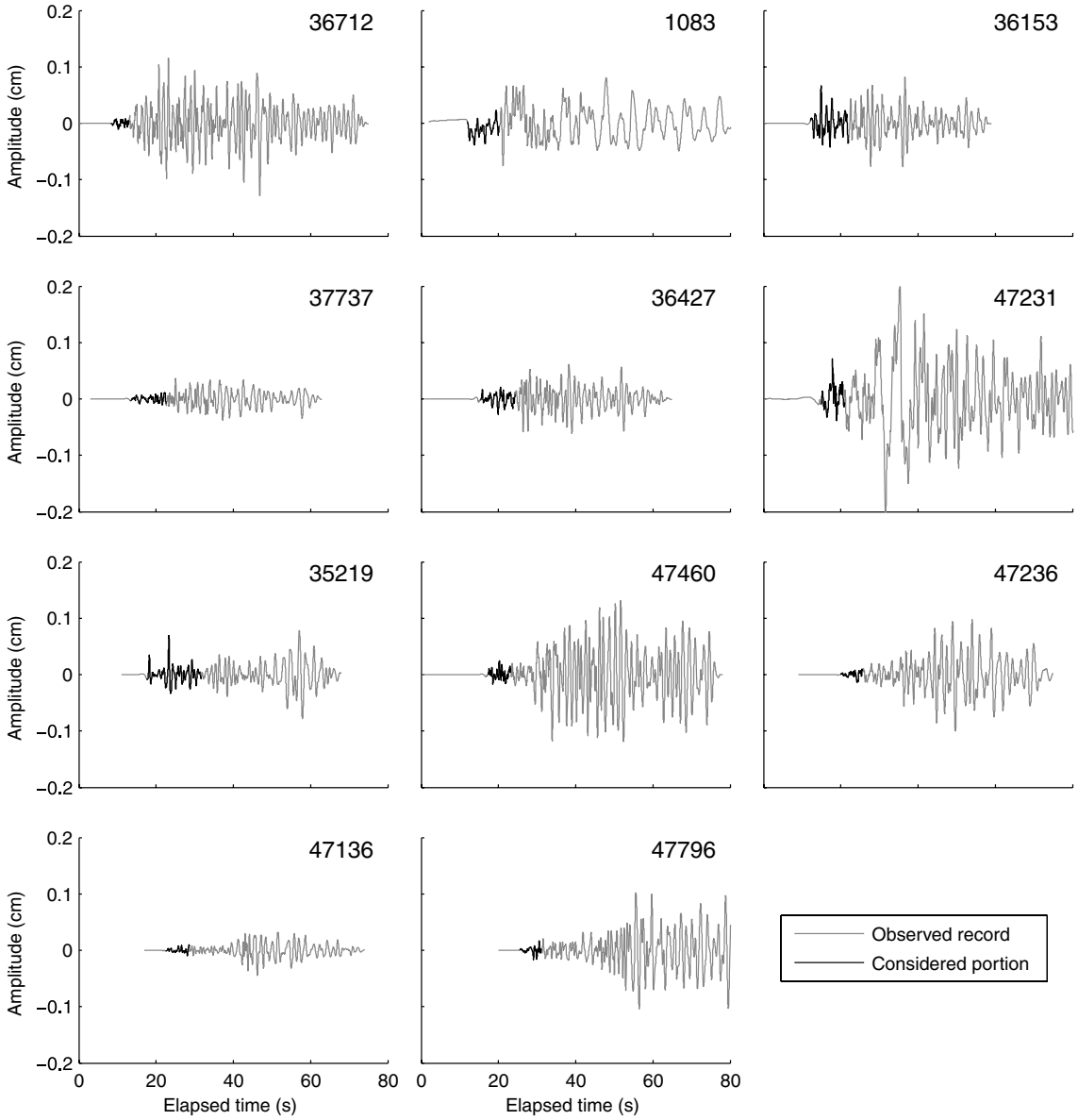

Figure 7. Vertical component displacement records for all the stations that were used in the *P*-phase BPM analysis. The entire record is shown in grey and the portion of the record used in the analysis is shown in black.

of the region on either side of the fault plane (Thurber *et al.* 2004, 2006). Hence, different 1-D velocity models are used to calculate theoretical traveltimes for stations on southwest and northeast sides of the fault plane (Hartzell *et al.* 2007). The 1-D velocity models are given in the Table 1.

We recover the amplitude and distribution of slip along the Parkfield rupture plane by applying the BPM to the displacement records of both the *P* and *S* waves. First, we use *P*-wave energy recorded on vertical component seismograms to image the rupture. To back project the *P*-wave data, the records must have clear *P*-wave arrivals with a high signal-to-noise ratio. We use records from stations that are far enough from the epicentre to allow adequate separation between *P* and *S* arrivals and at distances small enough to avoid secondary phase arrivals (e.g. *P*-to-*S* converted waves). Based on these criteria, stations within a distance range from 40 to 150 km are suitable for back projection analysis of this rupture. A total of eleven stations are suitable for back projecting *P*-wave data after removing nearly colocated stations (see Fig. 6). Fig. 7 shows the vertical component seismograms recorded at these stations. Records were bandpass filtered between 0.1 and 8 Hz prior to computing the envelopes. Traveltimes between each grid cell along the fault plane and each seismic station are calculated using a 1-D velocity model, as described above. To account for variations in the isochrone times due to 3-D velocity structure, the traveltimes calculated from 1-D model are corrected using static time shifts (c_i). Envelopes are averaged using a window ($2W$) of 0.33s (approximately equal to the isochrone spacing between the adjacent grid points) to reduce the effect of any additional uncertainties in the traveltime estimates. The rupture time for each grid point is determined by assuming the rupture initiates at the hypocentre and propagates radially outward at a constant velocity of 2.8 km s^{-1}.

The final slip map after four iterations, estimated by back projecting the *P*-wave data, is shown in Fig. 8. The slip map shows slip is concentrated primarily in two regions along the fault plane; first,

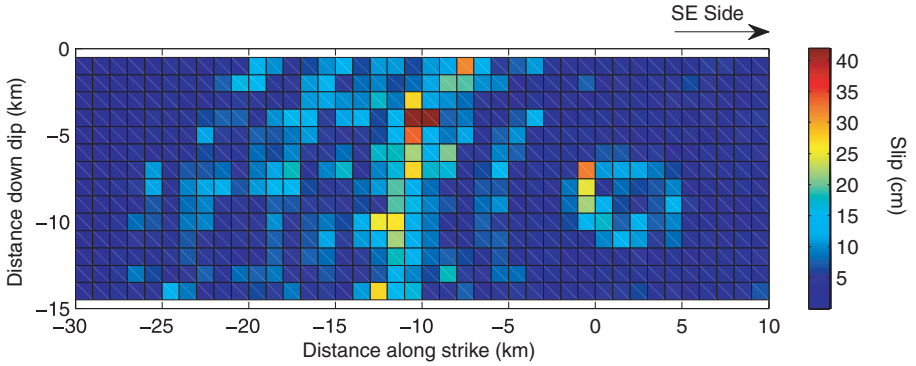

Figure 8. Slip map obtained by back projecting the *P*-wave envelopes after four iterations for the station distribution shown in Fig. 6.

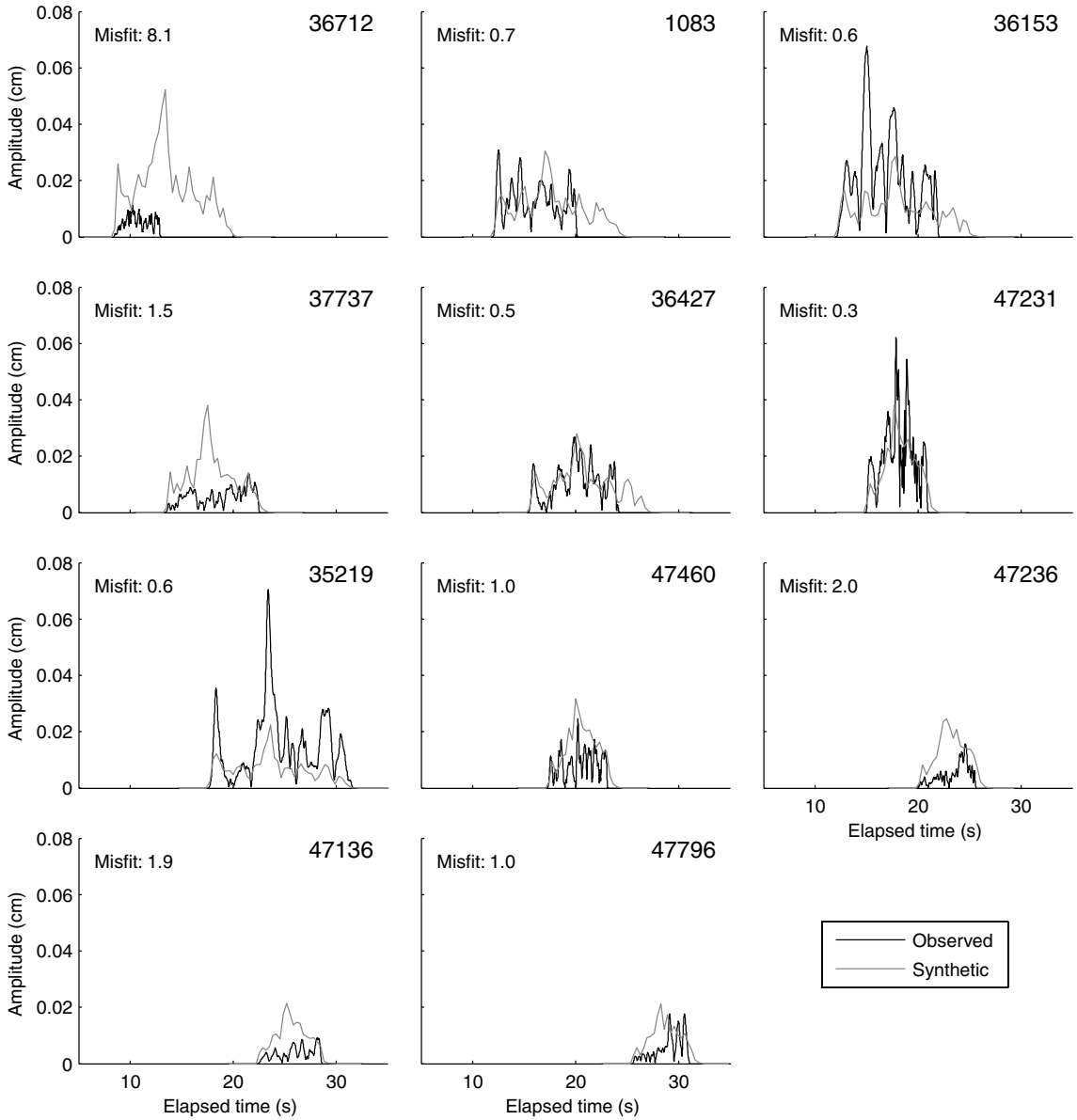

Figure 9. Comparison between the actual *P*-wave envelopes and back-calculated envelopes after the fourth iteration for each station. Numbers in the top right corner of the figures denote the station numbers as shown on Fig. 6.

Table 2. Average misfit after each iteration in the analysis for different seismogram components.

Component	Iteration I	Iteration II	Iteration III	Iteration IV
Vertical	1.56	1.60	1.63	1.66
Radial	1.04	1.01	0.98	0.96
Transverse	1.11	1.08	1.07	1.07

about 30 cm of slip occurs at the hypocentre and, second, an additional 40 cm of slip occurs approximately 10 km northwest of the hypocentre. However, smearing of the energy is observed near the second asperity due to a paucity of intersecting isochrones from the available stations. Fig. 9 shows the observed and back-calculated envelopes after four iterations. Table 2 provides the average misfit between the actual and back-calculated envelopes after each of the four iterations. The average misfit increases slightly with successive iterations, likely due to a large amplitude pulse on a highly weighted station (Station 35219). This station seems to require more slip at −10 km from hypocentre at a depth of 5 km that is not supported by the data from other stations. The slip averaged over the entire fault length is 5.94 cm and is comparable to the average value of slip (5.8 cm) determined from the moment magnitude (9.8×10^{24} dyne-cm (http://www.cisn.org/special/evt.04.09.28/nc51147892.mt) of the Parkfield earthquake, using the reported fault dimensions (40 km × 14 km) and a typical rigidity ($\mu = 3.0 \times 10^{11}$ dyne cm^{-2}).

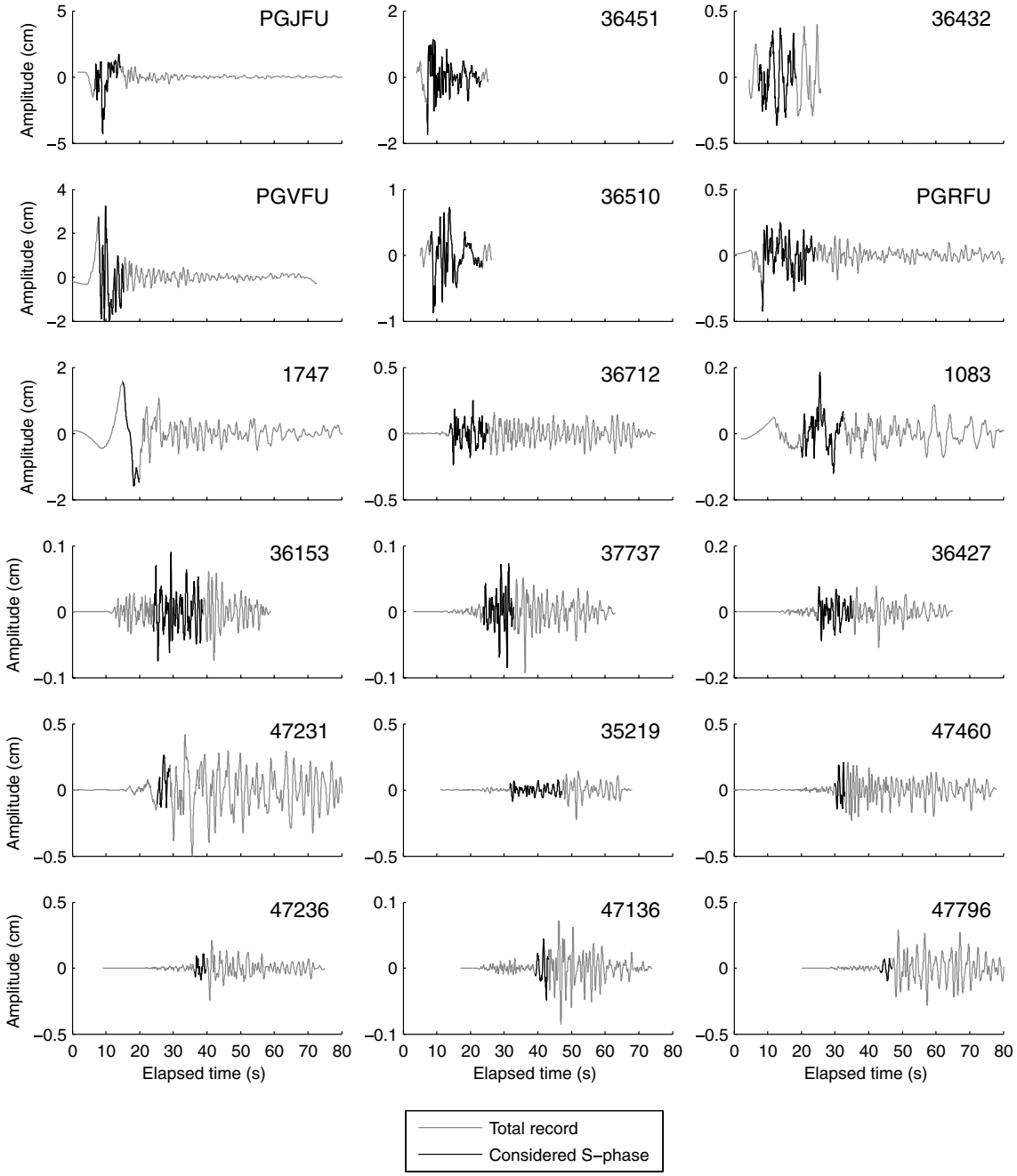

Figure 10. Radial displacement records for all stations that were used in the *S*-phase BPM analysis. The entire record is shown in grey and the portion of the record used in the analysis is shown in black.

To further refine the slip distribution of the Parkfield rupture, we back project the *S*-phase waveform data. We include data from stations at least 15 km away from the epicentre to minimize the influence of *P*-wave coda on the *S*-wave envelopes. A total of eighteen stations are within 15–150 km distance and azimuthally well-distributed around the rupture (Fig. 6). The horizontal records were rotated to the radial and transverse directions and then bandpass filtered from 0.2 to 8 Hz. The radial displacement records and a comparison of the back calculated and observed envelopes of the radial component data, after the fourth iteration, are shown in Figs 10 and 11. The final slip maps determined from the radial and transverse components, using a similar method as described above for the *P*-wave data, are shown in Figs 12(a) and (b). The final slip distribution is constructed by summing the slip images determined for the radial and transverse components and is shown in Fig. 12(c). The average misfit after each iteration is given for both radial and transverse components in Table 2. In the resulting rupture image determined from *S*-phase waveforms, we observe two regions of high slip. The first region, with 35 cm of slip, is centred on the hypocentre and the second, with 23 cm of slip, is located 15 km northwest of the hypocentre at approximately 5–10 km depth. The fit between the observed and back-calculated envelopes (Fig. 11) is

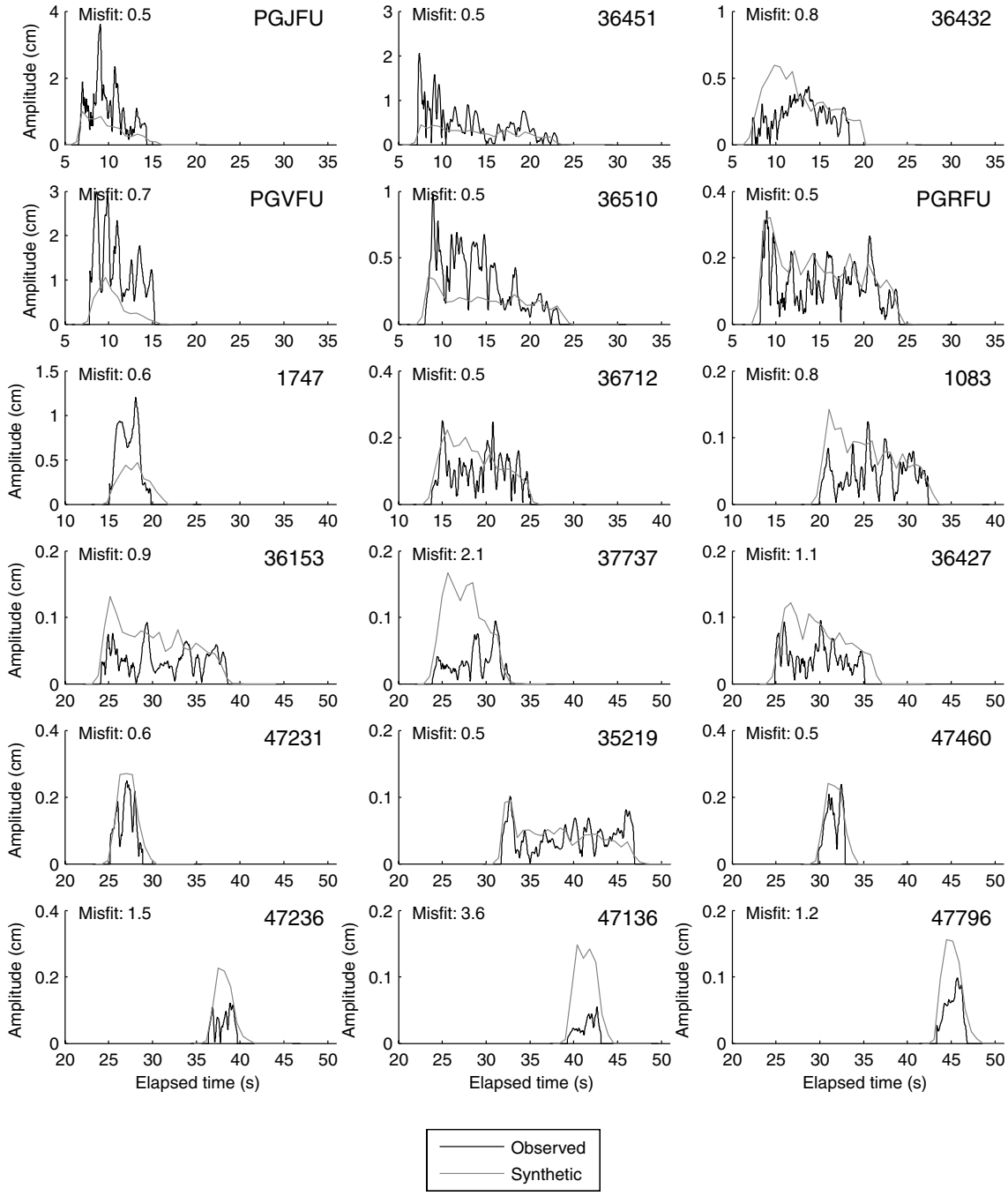

Figure 11. Comparison between the actual and back-calculated envelopes after the fourth iteration for radial component data.

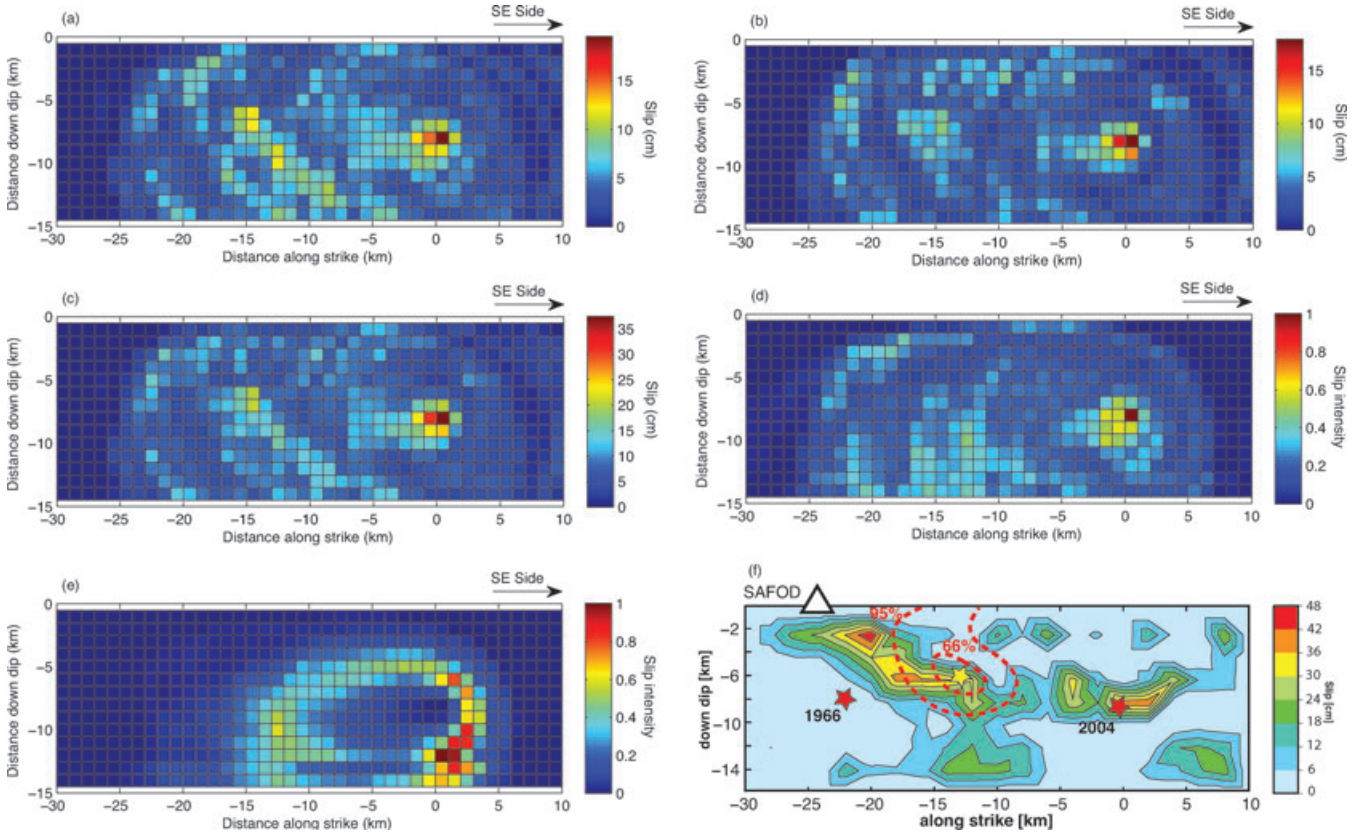

Figure 12. Final slip maps obtained after four iterations by back projecting the envelopes of the radial and transverse components, the *S*-wave envelopes for the station distribution shown in Fig. 6. (a) Using radial components. (b) Using transverse components. (c) Combined slip map from both radial and transverse components to represent the slip map from *S* phase. (d) Slip map obtained implementing Pulido *et al.* (2008) method and following iterative procedure similar to our method. (e) Slip map obtained implementing a similar iterative procedure to Pulido *et al.* (2008). (f) Slip distribution from Liu *et al.* (2006) inversion model, with the location of the secondary high slip region identified by Allmann & Shearer (2007) marked in red dotted lines (from Allmann & Shearer 2007).

good for most of the stations and the average misfit is reduced with successive iterations (Table 2). The average slip over the fault area is observed to be 6.32 cm.

6.1 Comparison of slip maps between *P* and *S* phase, and with other studies on the Parkfield

As discussed above, the slip map determined from *P*-phase waveforms has some energy smearing across the entire fault depth at 10 km northwest of the hypocentre resulting from similar isochrone distributions for several stations (e.g. Fig. 1). In addition, the large slip amplitudes in this region may be due to a particularly high amplitude pulse at station 35219 around 23.4 s. Station 35219 also has a relatively high station distribution weight because no other station is at a similar backazimuth. This smearing of energy is not observed in the slip maps determined using *S*-phase data because there is a better spatial distribution of stations with distinctive isochrones.

Further, we compare our results to the slip maps previously published for the M_w 6.0 2004 Parkfield earthquake determined using the source inversion (e.g. Custódio *et al.* 2005; Liu *et al.* 2006; Hartzell *et al.* 2007) and other back projection implementations (Allmann & Shearer 2007; Kao & Shan 2007; Pulido *et al.* 2008). Most models of the Parkfield rupture identify two main asperities: one at the hypocentre and a second at a distance of 10–20 km northwest of the hypocentre. Fig. 12(f) (from Allmann & Shearer 2007) presents the best slip map from Liu *et al.* (2006) determined by averaging the ten best rupture scenarios from source inversions. Fig. 12(f) also illustrates the secondary high slip region (outlined by the red dotted lines) identified by Allmann & Shearer (2007).

The slip map we determined using *S*-phase waveforms provides a more focused image of the slip distribution and is comparable to slip maps determined in previous studies of the Parkfield rupture. As outlined above, there are two high slip regions (asperities); one asperity is located at the hypocentre with a slip amplitude of 35 cm and the other asperity located 15 km NW of the hypocentre at a depth of 6 km, with a slip amplitude of 23 cm. The slip amplitude at the hypocentre is similar to that determined by Liu *et al.* (2006), but the slip amplitude at the second asperity is reduced by approximately 10–20 cm. Our slip image show some slip at multiple locations across the fault plane, away from the two high slip regions, which are also similar in distribution and amplitude to the slip shown by Liu *et al.* (2006). A few moderate to low slip regions, such as the one at 5 km NW of the hypocentre at 15 km depth do not match the results of Liu *et al.* (2006). These slip regions may be real or artefacts in the slip map due to smearing of the energy along an isochrone or because we back project the whole time series rather than individual time slices.

We also provide the slip maps obtained by applying the method of Pulido *et al.* (2008) to the Parkfield event in Figs 12(d) and (e). We present two implementations of the Pulido *et al.* (2008) method as it is not clear how successive iterations are computed. The slip map in Fig. 12(d) is obtained using the same iteration method that we use in our method, for example, the amplitude of the envelope is back

projected onto the fault along the isochrones. As shown in Fig, 12(d), the resulting slip map has energy smeared along the isochrones with the result dominated by stations with similar isochrone distributions. This was addressed in our method by introducing a factor to correct for non-uniform station distribution. The slip map shown in the Fig. 12(e) is an implementation of the Pulido *et al.* (2008) method that scales the slip intensities for successive iterations by the maximum intensity of the previous slip maps.

We are unable to quantitatively compare our results with earlier applications of the BPM to the Parkfield earthquake (e.g. Allmann & Shearer 2007; Kao & Shan 2007). For example, Allmann & Shearer (2007) examined specific time slices from the rupture and only presented slip maps for specific time periods of the rupture process. Thus, they do not have a single, final slip map that can be used for comparison. Defocusing of the energy is observed in their results; as they discuss, when they align records to the origin time to determine the slip at the hypocentre, the secondary asperity location becomes defocused. Similarly, when they align records with the secondary asperity arrival, they did not observe any energy at the hypocentre. We are unable to directly compare our results with Kao & Shan (2007), as their main objective was to identify the orientation of the fault plane, not the asperity locations.

6.2 Slip maps using subsets of stations

The synthetic tests shown in Section 5 suggest that slip amplitude and distribution can be adequately recovered using as few as four stations well distributed around the earthquake source. Here, we determine if the slip map of the Parkfield earthquake can be recovered using a small subset of the stations with good spatial distribution around the source. In addition, this test allows us to examine which slip features are consistent for different station subsets, and thus more reliable. We selected three station subsets and applied the BPM to recover the slip maps (Fig. 13). The slip maps for each of the three subsets are roughly similar and show some consistency with the slip map computed using all eighteen stations (Fig. 12a). However, the slip maps determined using the stations subsets have greater smearing of the asperities and some inconsistent regions of slip across the fault plane. The individual station subsets provide inferior slip images due to the increased influence of local site

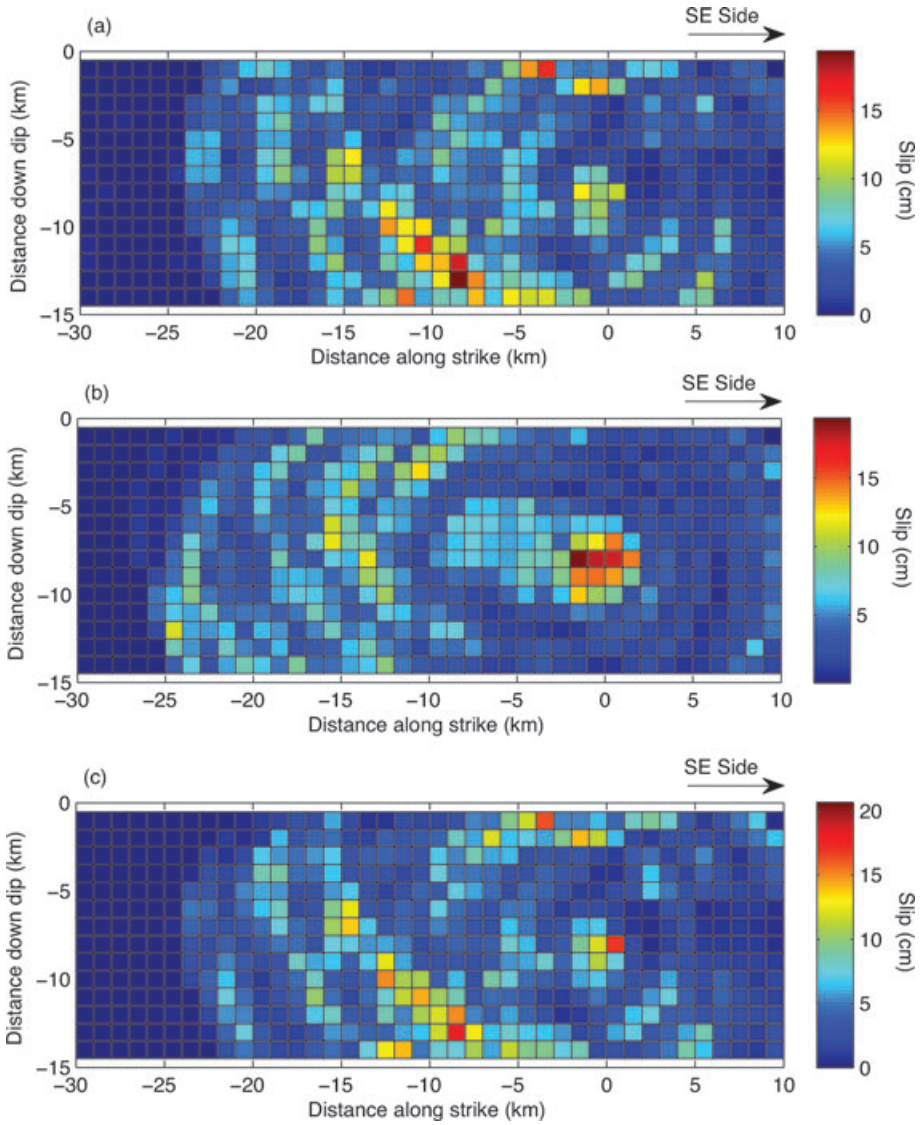

Figure 13. Slip maps determined using different station subsets. (a) Using stations PGJFU, 47231, 37737, 1083 and 36510, (b) using stations PGVFU, 47136, 36712, PGRFU and 35219 and (c) using stations 36510, 36427, 36432, 47236 and PGJFU.

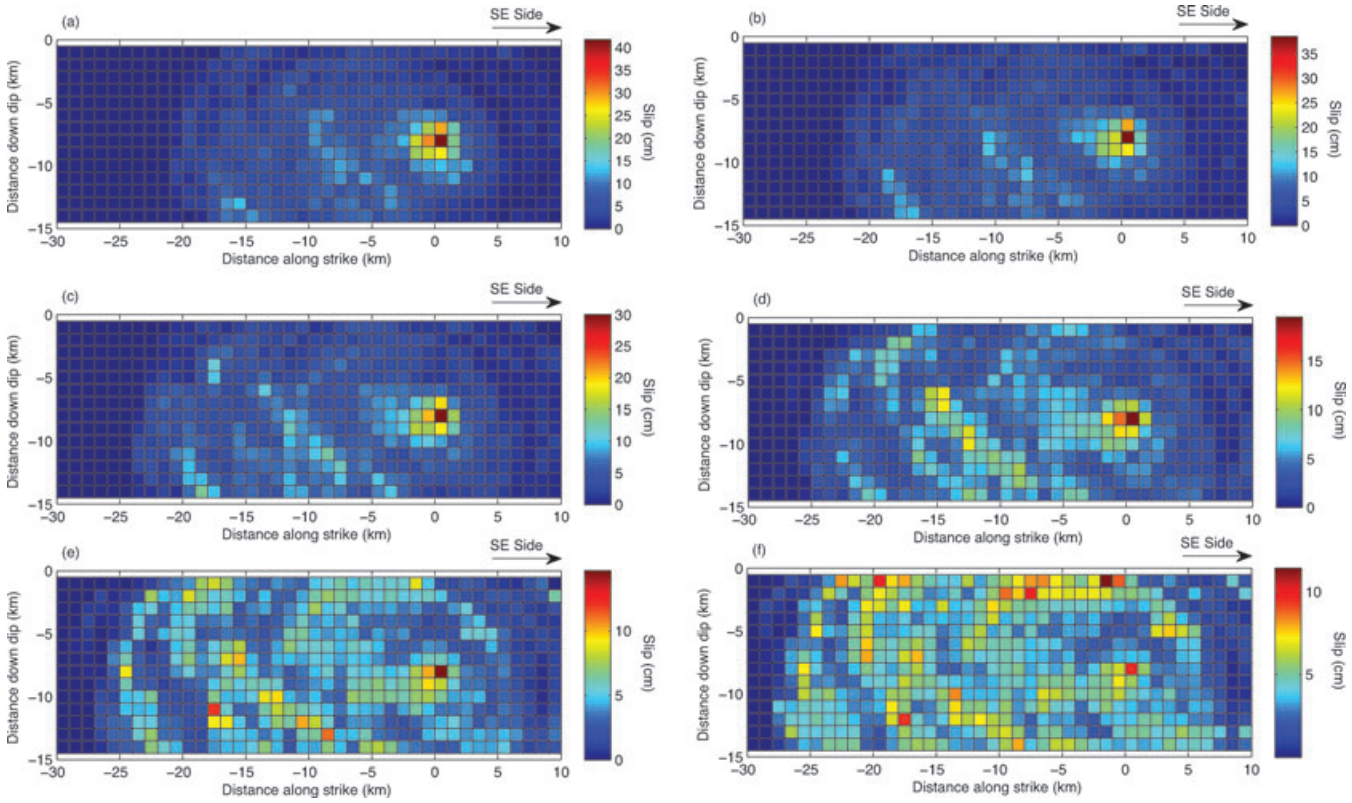

Figure 14. Slip maps for different rupture velocities: (a) 2.2 km s^{-1}, (b) 2.4 km s^{-1}, (c) 2.6 km s^{-1}, (d) 2.8 km s^{-1}, (e) 3.0 km s^{-1} and (f) 3.2 km s^{-1}.

effects. By using a large number of stations it is possible to minimize the influence of local site effects because the final slip map averages the observations from all of the stations.

6.3 Rupture velocity estimation

All of the results shown above were obtained by assuming a rupture velocity of 2.8 km s^{-1}. To confirm the rupture velocity for the Parkfield earthquake we back projected the radial component *S*-phase envelopes using a range of rupture velocities from 2.2 to 3.2 km s^{-1}. The resulting slip images are shown in Fig. 14. It is clear from these slip maps that a rupture velocity of 2.8 km s^{-1} results in a better slip map than the other rupture velocities tested. When rupture velocity is above 2.8 km s^{-1}, defocusing occurs and reduces the amplitude of slip at the asperities. And, when rupture velocity is less than 2.8 km s^{-1}, the slip at locations away from the hypocentre decreases significantly. The average misfits for each assumed rupture velocity after the 4th iteration are given in Table 3. Though the average misfits do not differ significantly, a lower average misfit is observed for a rupture velocity of 2.8 km s^{-1}. The small variation in the average misfits between the different cases is due to the use of high frequency ground motions, errors from local site amplifications, and other numerical simplifications. Note that we implement the BPM with a constant rupture velocity, so we are unable to determine if the rupture velocity changes significantly during rupture propagation. However, the estimated rupture velocity is similar to those reported in previous studies (Borcherdt *et al.* 2006; Hartzell *et al.* 2007; Ma *et al.* 2008).

Table 3. Average misfits after the fourth iteration for different rupture velocities.

Rupture velocity (km s^{-1})	2.2	2.4	2.6	2.8	3.0	3.2
Average misfits	0.98	0.97	0.97	0.96	0.97	0.99

7 CONCLUSIONS

The BPM implemented here is easy to apply, computationally efficient, and provides a good estimate of the location and amplitude of slip asperities. Here we implement a modified version of the BPM that can be used to determine the slip distribution and amplitude, not just slip intensity. Using synthetic examples we studied the influence of station distribution on the resulting rupture image to determine the limitations of the method. We find that for successful application of the method, the azimuthal distribution of stations is more important than the absolute number of stations. For cases with stations distributed in all four quadrants around the source the method can accurately determine the asperity locations and amplitude. We introduce a non-uniform station distribution factor that can be used to prevent the final slip image from being dominated by a particular station cluster, resulting in the smearing of energy from a single asperity. Envelopes are averaged over short time windows to reduce the influence of errors in the estimated traveltimes and the influence of noise from scattered or secondary arrivals on the amplitude. The window width chosen should be sufficiently long to account for uncertainties in the velocity structure, for example, the window length should be greater than the maximum expected uncertainties in the traveltimes estimates.

The BPM is applied to the 2004 M_w 6.0 Parkfield earthquake using both *P*- and *S*- phase near source displacement records. The slip distribution and amplitude obtained from the *P*- and *S*-wave records are able to identify two main high slip regions. The first high slip region is located at the hypocentre and the second is located between 10 and 15 km northwest of hypocentre. Some smearing

across a range of fault depths is observed, especially when using *P* waves, mainly due to the lack of stations at a range of distances and azimuths around the source. It is clear that the application of BPM to a real earthquake, in contrast to the synthetic example, requires a larger number of stations distributed around the source to account for uncertainties in estimated traveltimes resulting from a complex velocity structure and variations in amplitudes due to local site amplification. We find close agreement between the resulting slip maps determined here using the BPM and those determined using traditional inversion methods. Thus, the BPM can be used to quickly determine the location and amplitude of slip asperities for moderate to large earthquakes. Due to simplicity of implementation and relatively fast computation, the BPM is a good candidate for rapid determination of rupture parameters.

ACKNOWLEDGMENTS

We would like to acknowledge the careful and constructive reviews by two anonymous reviewers. This research was supported by National Science Foundation Grants GEO-0753290 and GEO-0753435.

REFERENCES

Aki, K. & Richards, P.G., 2002. *Quantitative Seismology,* 2nd edn, pp. 704, University Science Books, Sausalito, CA, USA.

Allmann, B.P. & Shearer, P.M., 2007. A high-frequency secondary event during the 2004 Parkfield earthquake, *Science,* **318,** 1279–1283, doi:10.1126/science.1146537.

Bernard, P. & Madariaga, R., 1984. A new asymptotic method for the modeling of the near-field accelerograms, *Bull. seism. Soc. Am.,* **74,** 539–557.

Borcherdt, R.D., Johnston, M.J.S., Glassmoyer, G. & Dietel, C., 2006. Recordings of the 2004 Parkfield earthquake on the general earthquake observation system array: implications for earthquake precursors, fault rupture, and coseismic strain changes, *Bull. seism. Soc. Am.,* **96,** S73–S89, doi:10.1785/0120050827.

Custódio, S., Liu, P. & Archuleta, R.J., 2005. The 2004 M_w 6.0 Parkfield, California, earthquake: inversion of near-source ground motion using multiple data sets, *Geophys. Res. Lett.,* **32,** L23312, doi:10.1029/2005GL024417.

Festa, G. & Zollo, A., 2006. Fault slip and rupture velocity inversion by isochrone backprojection, *Geophys. J. Int.,* **166**(2), 745–756, doi:10.1111/j.1365-246X.2006.03045.x.

Hartzell, S., Liu, P., Mendoza, C., Ji, C. & Larson, K.M., 2007. Stability and uncertainty of finite-fault slip inversions: application to the 2004 Parkfield, California, earthquake, *Bull. seism. Soc. Am.,* **97,** 1911–1935, doi:10.1785/0120070080.

Hartzell, S.H. & Heaton, T.H., 1983. Inversion of strong ground motion and teleseimic waveform data for the fault rupture history of the 1979 Imperial Valley, California, earthquake, *Bull. seism. Soc. Am.,* **73,** 1553–1583.

Ishii, M., Shearer, P.M., Houston, H. & Vidale, J.E., 2005. Extent, duration and speed of the 2004 Sumatra-Andaman earthquake imaged by the Hi-net array, *Nature,* **435**(16), 933–936, doi:10.1038/nature03675.

Ishii, M., Shearer, P.M., Houston, H. & Vidale, J.E., 2007. Teleseismic *P* wave imaging of the 26 December 2004 Sumatra-Andaman and 28 March 2005 Sumatra earthquake ruptures using the Hi-net array, *J. geophys. Res.,* **112,** B11307, doi:10.1029/2006JB004700.

Kao, H. & Shan, S.-J., 2004. The source-scanning algorithm: Mapping the distribution of seismic sources in time and space, *Geophys. J. Int.,* **157**(2), 589–594, doi:10.1111/j.1365-246X.2004.02276.x.

Kao, H. & Shan, S.-J., 2007. Rapid identification of earthquake rupture plane using source-scanning algorithm, *Geophys. J. Int.,* **168**(3), 1011–1020, doi:10.1111/j.1365-246X.2006.03271.x.

Liu, P., Custódio, S. & Archuleta, R.J., 2006. Kinematic inversion of the 2004 M_w 6.0 Parkfield earthquake including an approximation to site effects, *Bull. seism. Soc. Am.,* **96,** S143-S158, doi:10.1785/0120050826.

Luetgert, J.H., 1992. MacRay – Interactive two-dimensional seismic ray-tracing for the Macintosh, *U.S. Geological Survey Open File Rep.*, pp. 92–356.

Ma, S., Custódio, S., Archuleta, R.J. & Liu, P., 2008. Dynamic modeling of the 2004 M 6.0 Parkfield, California, earthquake, *J. geophys. Res.,* **113,** B02301, doi:10.1029/2007JB005216.

Olson, A.H. & Apsel, R.J., 1982. Finite faults and inverse theory with applications to the 1979 Imperial Valley earthquake, *Bull. seism. Soc. Am.,* **72,** 1969–2001.

Pulido, N., Aoi, S. & Fujiwara, H., 2008. Rupture process of the 2007 Notohanto earthquake by using an isochrones back-projection method and K-NET/KiK-net data, *Earth Planets Space,* **60,** 1–6.

Sekiguchi, H., Irikura, K. & Iwata, T., 2002. Source inversion for estimating the continuous slip distribution on a fault—introduction of Green's functions convolved with a correction function to give moving dislocation effects in subfaults, *Geophys. J. Int.,* **150**(2), 377–391, doi:10.1046/j.1365-246X.2002.01669.x.

Shakal, A., Glaizer, V., Huang, M., Borcherdt, R., Haddadi, H., Lin, K., Stephens, C. & Roffers, P., 2005. Preliminary analysis of strong-motion recordings from the 28 September 2004 Parkfield, California earthquake, *Seism. Res. Lett.,* **76,** 27–39.

Shearer, P.M., 2009. *Introduction to Seismology,* 2nd edn, pp. 260–262, Cambridge University Press, Cambridge, UK.

Spudich, P. & Frazer, N.L., 1984. Use of ray theory to calculate high-frequency radiation from earthquake sources having spatially variable rupture velocity and stress drop, *Bull. seism. Soc. Am.,* **74,** 2061–2082.

Thurber, C., Roecher, S., Zhang, H., Baher, S. & Ellsworth, W., 2004. Fine-scale structure of the San Andreas fault zone and location of the SAFOD target earthquakes, *Geophys. Res. Lett.,* **31,** L12S02, doi:10.1029/2003GL019398.

Thurber, C., Zhang, H., Waldhauser, F., Hardebeck, J., Michael, A. & Eberhart-Phillips, D., 2006. Three-dimensional compressional wavespeed model, earthquake relocations, and focal mechanisms for the Parkfield, California, region, *Bull. seism. Soc. Am.,* **96,** S38-S49, doi:10.1785/0120050825.

Walker, K.T., Ishii, M. & Shearer, P.M., 2005. Rupture details of the 28 March 2005 Sumatra M 8.6 earthquake imaged with teleseismic *P* waves, *Geophys. Res. Lett.,* **32,** L24303, doi:10.1029/2005GL024395.

Wang, G.-Q., Tang, G.-Q., Jackson, C.R., Zhou, X.-Y. & Lin, Q.-L., 2006. Strong ground motions observed at the UPSAR during the 2003 M 6.5 San Simeon and 2004 M 6.0 Parkfield, California, earthquakes, *Bull. seism. Soc. Am.,* **96,** S159–S182, doi:10.1785/0120050802.

SUPPORTING INFORMATION

Additional Supporting Information may be found in the online version of this article:

Supplement. Calculation of non-uniform station distribution factor, s_i.

Please note: Wiley-Blackwell are not responsible for the content or functionality of any supporting materials supplied by the authors. Any queries (other than missing material) should be directed to the corresponding author for the article.